https://doi.org/10.5194/essd-2025-715
Preprint. Discussion started: 13 January 2026

Open Access Earth System Science Data Discussions

Earthquake Catalog and Continuous Waveforms from a Two-Week Distributed Acoustic Sensing experiment on Kefalonia Island, Greece.

Gian Maria Bocchini[1], Emanuele Bozzi[2], Marco P. Roth[1], Sonja Gaviano[3], Giulio Pascucci[2], Francesco Grigoli[2], Ettore Biondi[4], Efthimios Sokos[5], Rebecca M. Harrington[1]

[1]Institute of Geosciences, Ruhr University Bochum, Bochum, Germany.
[2]Department of Earth Sciences, University of Pisa, Pisa, Italy.
[3]Seismix srl, Palermo, Italy.
[4]Stanford University, Geophysics Department, 397 Panama Mall, Stanford, CA 94305, USA.
[5]Department of Geology, Seismological Laboratory, University of Patras, Patras, Greece.

Correspondence to: Gian Maria Bocchini (gian.bocchini@rub.de)

Abstract. This work presents a high-resolution earthquake catalog for the Kefalonia region, Greece, built from the analysis of Distributed Acoustic Sensing (DAS) data recorded on a telecommunications cable between 1 August 2024, 23:00 and 15 August 2024, 23:00, together with open-access seismic station recordings. The DAS data consist of continuous strain recordings on a 15 km-long telecommunication optical fiber connecting northern Kefalonia and Ithaki. We use a semblance-based detector on the DAS waveforms to identify 5,734 earthquakes within ~50 km of the fiber origin. We jointly locate 284 high-SNR events with DAS and seismic stations and calculate their local magnitudes from seismic records. We then apply waveform cross-correlation to match unlocated detections with the most similar template events and estimate relative magnitudes from amplitude ratios to enhance the constructed catalog. Enhancement adds 2,496 earthquakes, resulting in 2,780 events with assigned locations and magnitudes. Most events (2,718) cluster within a ~5 km radius offshore northwest of Kefalonia, where seismicity rates reach >100 events per hour. Our dataset provides a detailed spatio-temporal view of seismicity in a region with limited station coverage and demonstrates the value of integrating DAS with conventional seismic networks to monitor intense earthquake sequences. The combination of high seismicity and open-access data from the Hellenic Unified Seismic Network makes this DAS dataset particularly valuable for the seismological community. We provide a 2-week-long catalog, the full detection list (local and distant events and false detections), and two weeks of continuous DAS recordings. The aim is to provide a resource for researchers to test, develop, and benchmark DAS processing algorithms on tectonic earthquakes and to investigate the physical processes that drive complex seismic sequences.

https://doi.org/10.5194/essd-2025-715
Preprint. Discussion started: 13 January 2026

1 Introduction

1.1 Why a new open-access dataset of DAS records?

Distributed Acoustic Sensing (DAS) has become an increasingly innovative approach in seismology to enable effective continuous spatiotemporal sampling of the recorded seismic wavefield through strain or strain-rate measurements on fiber optic cables (Zhan, 2020). The dense sampling has proven particularly well suited for applications that include seismic and microseismic monitoring (Glubokovskikh et al., 2023; Lellouch et al., 2021; Lindsey et al., 2017; Lior et al., 2021a; Porras et al., 2024), seismic imaging (Biondi et al., 2023a; Zeng et al., 2017), earthquake source-parameter estimation (Li et al., 2023; Lior et al., 2021b), monitoring of volcanic activity (Currenti et al., 2023; Jousset et al., 2022; Li et al., 2025), among others. Nevertheless, despite its rapid adoption, several factors still limit the broader exploitation of DAS data. The high sampling rates and density of measurement points generate large volumes of data introduce challenges to effective data storage and sharing (Seguí et al., 2025). Moreover, because DAS technology is still relatively new in seismology, many aspects of data processing and interpretation remain under active development, including seismic event detection and location, signal enhancement, strain-to-ground-motion calibration, and earthquake source parameter analysis. A further limitation is that most large publicly available DAS datasets are mainly related to microseismic monitoring of industrial operations (e.g., hydraulic stimulations) rather than natural seismicity, as technology evolved from industry. While several open-access datasets dedicated to the monitoring of natural earthquakes are present, they often lack elevated seismic rates and/or data from permanent seismic networks to augment the DAS experiment. The capability of using publicly available DAS datasets for the analysis of highly productive seismic sequences remains limited, slowing the validation and generalization of emerging data analysis methods across different tectonic contexts. Among the DAS datasets now publicly available (as of September 2025), PubDAS provides a repository with data from a variety of experiments, including natural and induced seismicity (Spica et al., 2023). The collection spans urban noise monitoring, volcanic environments, underground mines, and teleseismic events (Spica et al., 2023). FORGE (Frontier Observatory for Research in Geothermal Energy) (Pankow, 2022) and PoroTomo (Feigl et al., 2016) offer DAS data closely tied to geothermal research, including microseismicity monitoring related to hydraulic stimulation operations and subsurface characterization. Greenland Calving-Front Dataset offers a demonstration of the DAS and DTS potential in cryospheric research (Gräff et al., 2025). The Global DAS Month of February 2023 dataset (Wuestefeld et al., 2024) comprises globally coordinated DAS recordings acquired to advance efforts toward a Global Fiber Sensing Network and promote standardized, collaborative seismic monitoring.

Here we present a new dataset of DAS recordings that captured a natural seismic sequence along the Kefalonia transform fault system, in Greece. The seismic sequence occurred approximately at 15 km epicentral distance from the interrogated cable, along with other natural earthquakes in the region. In addition to DAS data, a set of permanent seismic stations in close proximity provides an augmented data set to enable integration of DAS and seismic station data, which, to date, remains relatively unexplored. In the following, we present a new earthquake catalog that covers a two-week period coinciding with elevated seismicity, as well as the continuous DAS waveforms used to build the catalog. We also document

https://doi.org/10.5194/essd-2025-715
Preprint. Discussion started: 13 January 2026

the publicly available station data that we use to augment the DAS data to gain a significantly detailed seismicity catalog in a natural tectonic setting. As detailed in the following section, the activity clustered offshore northwest of Kefalonia, at about 10 km from the fiber's starting point (Fig. 1), and includes additional earthquakes at distances of up to ~50km. The seven open-access permanent seismic stations from the Hellenic Unified Seismic Network (HUSN) are located within ~30 km of the fiber's starting point. The dataset released with this paper is useful not only to researchers developing DAS data-analysis methods, but also to those studying earthquake physics and statistical seismology. Our analysis highlights the benefits of combining DAS and seismic station data to examine seismicity features in greater detail in a natural tectonic setting.

1.2 The Kefalonia Transform Fault and the 2024 seismic sequence

The Kefalonia Transform Fault (KTF) is a major tectonic structure in the Eastern Mediterranean that marks the transition from oceanic subduction to the south to continental collision to the north (Bocchini et al., 2018; Louvari et al., 1999; Royden and Papanikolaou, 2011; Scordilis et al., 1985). The KTF accommodates 2–2.5 cm/yr of differential convergence between the oceanic subduction and continental collision zones (Pérouse et al., 2012), making it one of the most seismically active faults in Europe, as evidenced by frequent M6–7+ earthquakes (Papadimitriou, 2002). A period of increased seismic activity started offshore northwest of Kefalonia at the end of February 2024 and lasted until the end of the year. The largest magnitude earthquakes (M_L3.6-3.8) occurred in the first weeks of March 2024, and earthquakes with $M_L > 3.0$ were also recorded in April, August, and October 2024 (https://bbnet.gein.noa.gr/HL/databases/database). Anagnostou et al. (2025) present an analysis of the activity during the period of February-April 2024 and interpret the sequence as being complex with swarm-like behavior, highlighting the important role of fluids in its triggering. Notably, the authors report that the primary structure(s) that were activated include WNW-ESE left-lateral strike-slip fault(s), rather than the main branch of the KTF.

1.3 Description of the DAS experiment in Kefalonia and goal of this study.

We used Distributed Acoustic Sensing (DAS) to measure strain along a dark telecommunications optical fiber connecting the islands of Kefalonia and Ithaki, in the Ionian Sea (Greece) (Fig. 1). The fiber starts in the village of Antipata (Kefalonia), runs inland for slightly more than half of its ~15.5 km length, crosses the Strait of Ithaki over steep bathymetry, and terminates in the village of Stavros (Ithaki) (Fig. 1). The DAS measurement period ranges from early July to late September 2024, where we recorded continuous data using an OptaSense QuantX interrogator. In this study, we focus on a seismically active period identified from the revised catalog of the National Observatory of Athens (https://bbnet.gein.noa.gr/HL/databases/database), spanning 2–15 August 2024 (1 August 23:00 – 15 August 23:00), to construct an enhanced earthquake catalog. We combine DAS strain recordings with continuous recordings of ground velocity from seven seismic stations of the HUSN to mitigate the azimuthal gap caused by the relatively short cable length, which is comparable to the epicentral distance between the cable and the recorded seismicity, and obtain higher quality earthquake locations than would be possible with DAS or seismic data alone. The complementary seismic data also enables more accurate magnitude estimations, which are hindered by the lack of a calibrated instrument response for converting

https://doi.org/10.5194/essd-2025-715
Preprint. Discussion started: 13 January 2026

strain to displacement (Lior et al., 2021b). In other words, complementing the DAS with seismic station data enables building a high-quality, manually revised earthquake catalog during the two-week study period. One main objective of this work is to publicly release the dataset to provide the community with an opportunity to test, benchmark, and develop methods for detecting and locating earthquakes with both DAS data and hybrid DAS-seismic station networks using a productive, tectonic seismic sequence. Moreover, the dataset offers the opportunity to investigate the statistical features and underlying physical mechanisms driving complex seismic sequences.

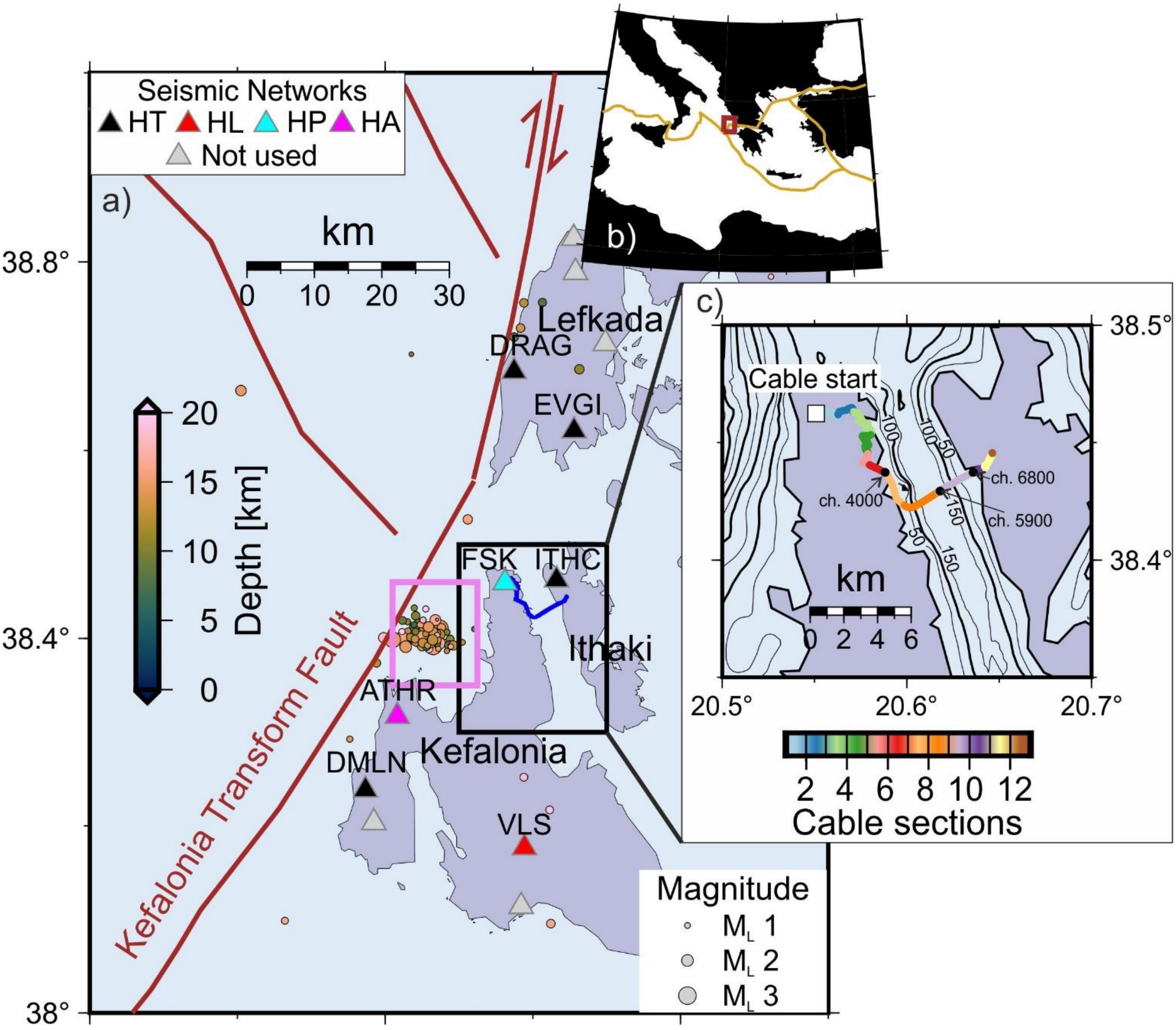

https://doi.org/10.5194/essd-2025-715
Preprint. Discussion started: 13 January 2026

Figure 1. (a) Map view of the study region, including the location of the optical fiber, seismic events (colored circles) reported by the National Observatory of Athens (https://bbnet.gein.noa.gr/HL/databases/database, last accessed September 2025), and the publicly available seismic stations from the Hellenic Unified Seismic Network (HUSN) used (colored triangles) to locate seismic events. Grey triangles indicate public seismic stations from the HUSN not used in this study. Thick brown lines indicate major active faults (Basili et al., 2024). (b) Inset showing the location of the study region within the Central-Eastern Mediterranean Sea. (c) Zoom on the optical fiber. The optical fiber is divided into 12 segments (see methods) that are used for earthquake location. Continuous black lines indicate isobaths. Black circles along the cable indicated the position of channels (ch.) mentioned in the text.

2 Data

We recorded DAS data with a temporal sampling rate (i.e., ping rate) of 5000 Hz, which we decimated by a factor of 20 before storing them, yielding a sampling rate of 250 Hz. The system configuration has a gauge length of 10 m and a channel spacing of 2.04 m, resulting in a total of 7,750 channels. Data is saved in 30-second segments (~80 MB per file), resulting in a total size of 3.1 TB for the two-week experiment, with a short gap in data archiving occurring between 09:14 and 09:48 on the 6th of August 2024. The file name is UTC time + 1h (default naming from the system).

We performed tap tests on both Kefalonia and Ithaki islands to precisely identify the channel locations onshore. The cable onshore was visible along the entire length, where it had been covered by asphalt along streets. Offshore, the cable path and channel positions are less certain. We rely on the expected number of channels (after subtracting those onshore) and compare the moveout of earthquake P-wave arrivals (from earthquakes reported in the revised NOA catalog) with earthquake-to-channel epicentral distances (Fig. S1) to refine the cable location offshore. We employ EMODnet bathymetry (https://emodnet.ec.europa.eu/en/) to assign an elevation to the channels offshore, while for the onshore channels, we rely on the elevation from our GPS device. We also check for loops (typical of telecom infrastructures) in the onshore cable sections by analyzing the normalized energy recorded on each channel (Biondi et al., 2023b), and then cross-validating it with vehicle signals generated while driving along the fiber (Fig. S2). We show the locations of identified loops in Fig. 2 (gray areas between dashed vertical lines). Automatic picking of P-wave arrivals along the fiber resulted from applying PhaseNet-DAS (Zhu et al., 2023).

We perform an initial assessment of data quality by manually inspecting recordings of earthquakes within a ~50 km radius of the fiber starting point using the revised NOA catalog (M_L 0.5–3.4). The catalog lists 91 earthquakes (last accessed September 2025) within the two-week study period, all of which are clearly visible along the fiber (Fig. 2, Fig. S3). We observe that we can successfully record signals from teleseismic earthquakes, mostly on the offshore portion of the cable (Fig. S4). Earthquake recordings show strong amplification (a factor >20) in the offshore segment, while onshore and offshore maximum noise amplitudes are similar, with slightly higher noise amplitudes offshore (Fig. 2). Expected amplitude scaling with earthquake magnitude is also evident: for example, an amplitude ratio of ~230–240 between events of M_L 0.6 and M_L 3.0 located ~1.7 km apart (epicentral locations from NOA catalog) is consistent with the theoretical value of ~250 that is expected if the events were co-located (Fig. 2c). We also note consistently elevated amplitude signals at both the onshore–offshore transition zones of the cable (Fig. 2). The seven seismic stations of the Hellenic Unified Seismic Network

https://doi.org/10.5194/essd-2025-715
Preprint. Discussion started: 13 January 2026

(HUSN) that complement the DAS data include: FSK (HP, 2000), ATHR (HA, 2008), VLS (HL, 1975), EVGI, DLMN, ITHC, DRAG (HT, 1981) (Fig. 1, Fig. S3).

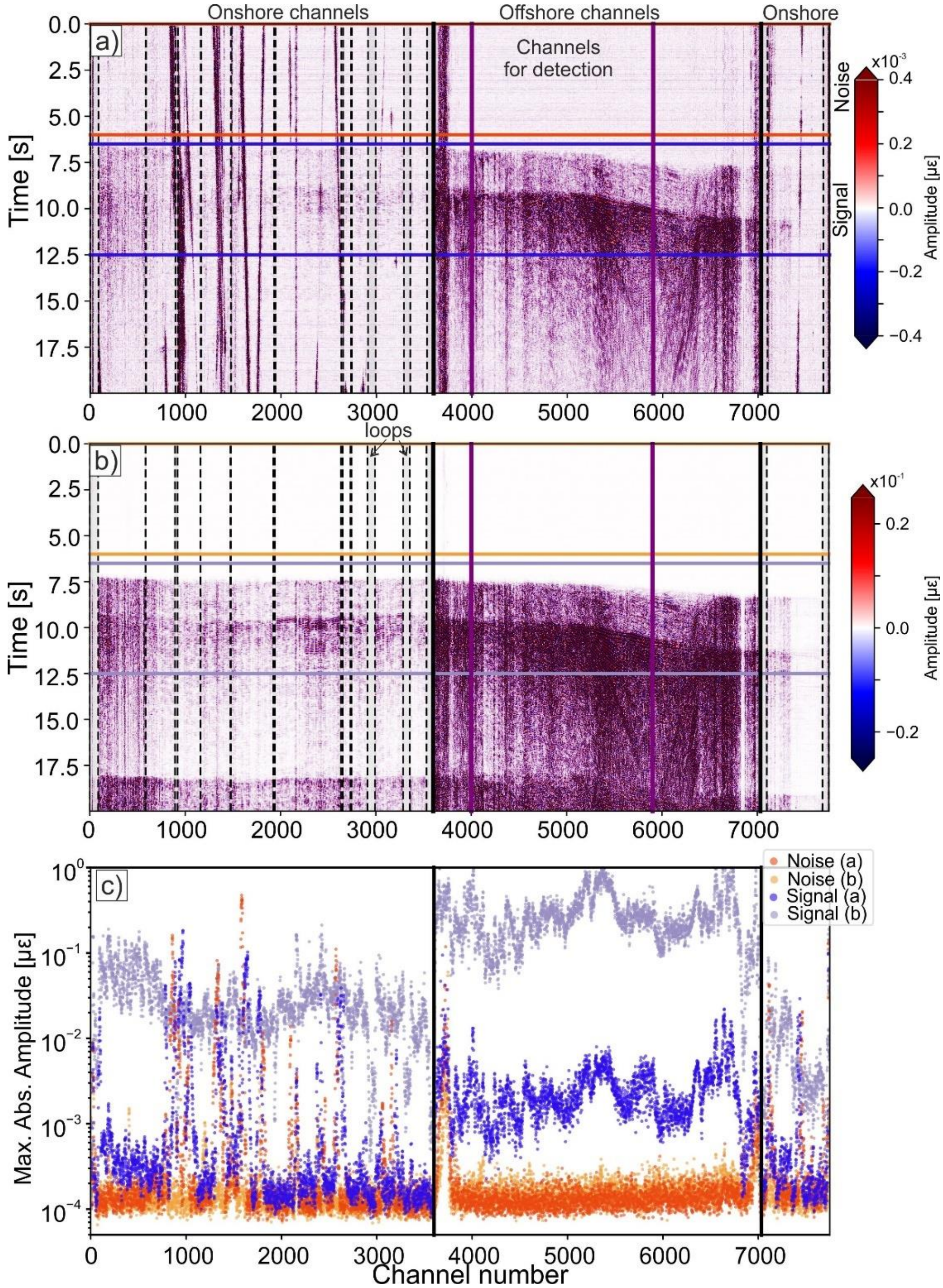

Figure 2. (a) Example of earthquakes recorded along the cable. (a) M_L 0.6 on 08 August 2024 at 10:35 UTC (NOA event-id: noa2024pmvwc). (b) M_L 3.0 Earthquake on 08 August 2024 at 19:18 UTC (NOA event-id: noa2024pnndk). (c) Maximum absolute amplitudes of signal and noise shown in panels (a-b). Panels (a-b) detail the location of onshore and offshore channels, the location

https://doi.org/10.5194/essd-2025-715
Preprint. Discussion started: 13 January 2026

of the channels used for the detection, and the location of the identified loops. Traces are bandpass filtered 5-30 Hz. The light and dark orange, and violet and blue lines in panels (a-b) highlight the noise and signal windows shown in panel (c).

3 Earthquake detection using DAS data.

We use a semblance-based earthquake detector, HECTOR, to detect earthquakes recorded along the optical fiber (Porras et al., 2024). The detector evaluates the coherence of the waveforms along pre-computed hyperbolic trajectories with varying curvature and vertex along the fiber and time axes (x-t) using a modified semblance function (Fig. 3). The run of the detector requires a set of pre-processing steps that include: (1) removing the mean and linear trend of each trace; (2) normalizing trace amplitudes to reduce the effect of geometrical spreading, fiber coupling, and nonlinear effects; (3) applying a bandpass filter of 5-30 Hz as well as a (4) common mode noise removal through frequency–wavenumber (fk) filter (i.e., removal of k=0).

Owing to the strong signal amplification offshore and the clearer hyperbolic seismic phase arrival moveouts, we perform the detection using an offshore segment of the fiber (Fig. 2). Testing different configurations led us to use channels 4000-5900 for detection (Fig. 1c, Fig. 2), corresponding to a total length of ~3900 m. Since the target seismicity cluster northwest of Kefalonia lies beyond the fiber's extent, we fix the hyperbola vertex at channel 4000 (bottom Fig 3c). We let the curvature of the hyperbola vary between 130-200° with steps of 5° and use temporal windows of 30 samples with steps of 10 samples to calculate the semblance and evaluate the coherence of the signals. We run the detection algorithm on 45-second data windows with a 15-second overlap (Fig. 3). The overlap ensures that potential earthquakes that might occur across two consecutive files are not missed. To avoid duplicate entries, we de-cluster the initial detection list by removing signals that occur within 3 seconds of each other and keep the earliest detection. We choose a 3-second threshold because the observed $T_S - T_P$ along the offshore channels (Fig. 2a-b) is ~2.5 seconds for earthquakes in the cluster northwest of Kefalonia. The detector is unable to distinguish between P- and S-waves, without additional processing this can lead to P- and S-waves from a given earthquake being classified as separate events. The 15-second overlap between consecutive windows may also cause the same event to be detected twice, which we also mitigate with the de-clustering. We note that detection time (Fig. 3a) may be shifted with respect to the phase arrival observed in Fig. 3c because the vertex and the curvature of the hyperbola provide the highest signal coherence, which may not be perfectly corresponds with the earliest time of the phase arrival.

https://doi.org/10.5194/essd-2025-715
Preprint. Discussion started: 13 January 2026

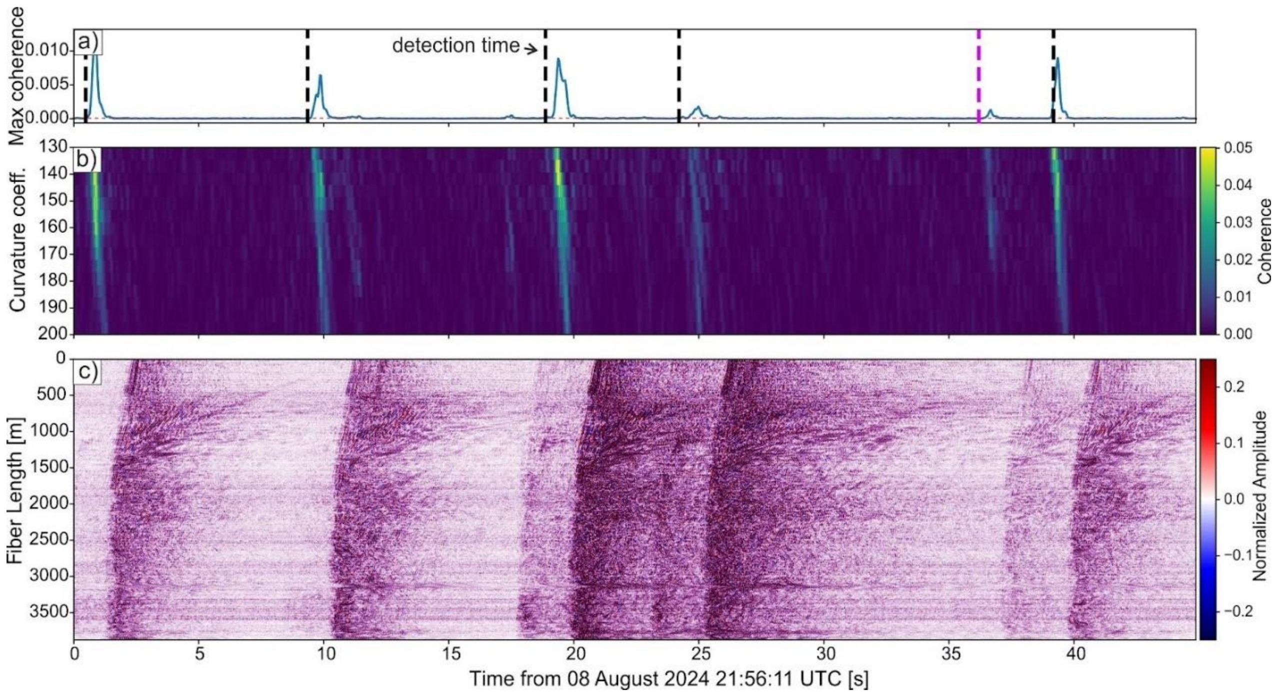

Figure 3. (a) Coherence time series in a 45-s window showing six detections. Vertical dashed black lines mark detection times. Violet vertical dashed line (second from the right) indicates a detection identified in the subsequent window (30–75 s) and not in the time window shown here (see text). (b) Semblance matrix, where the coherence maxima highlight events detected by HECTOR (Porras et al., 2024). (c) DAS recording with y-axis channels ranging from 4000 (bottom) to 5900 (top). See text for details of trace processing (Section 3). Note that detection times may mark the S-wave arrival, where P-waves are not always clearly visible.

Running the HECTOR detection algorithm on the 2-weeks of data leads to a total of 6,817 detections (Fig. 4). The number of detections increases substantially relative to the revised NOA catalog, with the highest counts occurring after M_L 2.5+ earthquakes listed in that catalog. (Fig. 4). The number of detections within 1-hour bins following M_L 2.5+ events from the NOA catalog exceeds 100 and exhibits an Omori-like decay (Fig. 4). We note that all M_L 2.5+ NOA earthquakes reported in Fig. 4 occurred within the active cluster northwest of Kefalonia (pink box in Fig. 1). Importantly, although we calibrate the detector parameters to maximize sensitivity to the region of elevated seismicity offshore northwest of Kefalonia Island, we successfully detect all 91 earthquakes reported in the NOA catalog that occurred within ~50 km of the fiber's starting point (Fig. 1). The sensitivity to various azimuthal directions, distances, and magnitudes suggests that the set of parameters, DAS channels, and waveform processing used in the detector (as applied in this study) offer sufficient flexibility.

https://doi.org/10.5194/essd-2025-715
Preprint. Discussion started: 13 January 2026

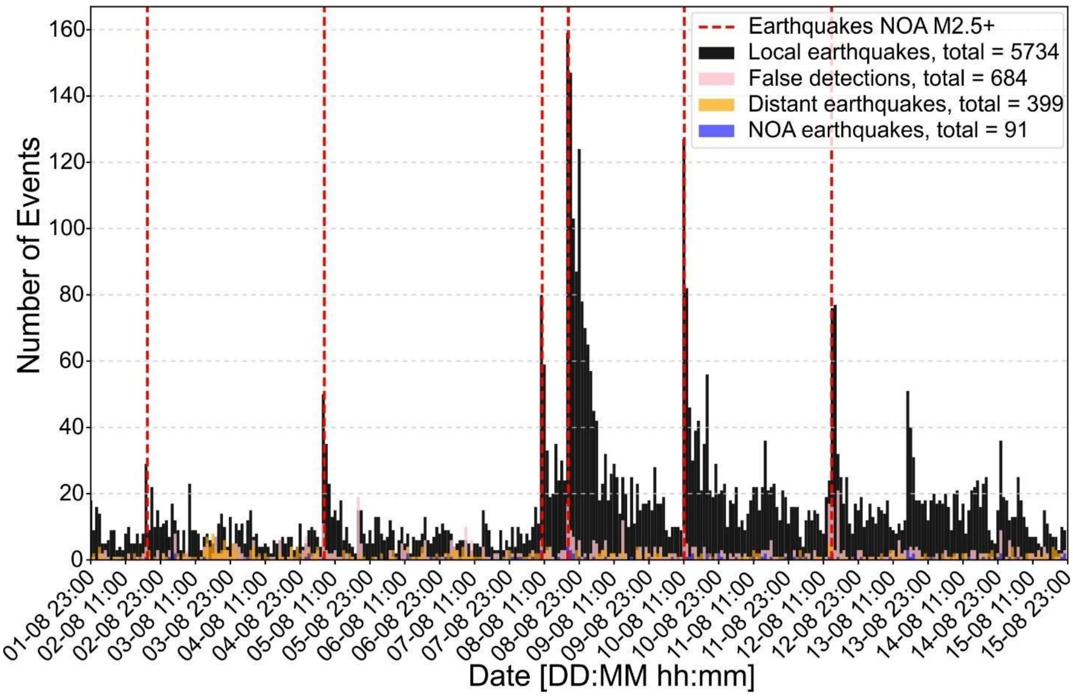

Figure 4. Histogram of detections with 1-hour bins obtained with HECTOR from 1 August 2024 at 23:00 to 15 August 2024 at 23:00. Detections are classified after manual inspection of the signals. Distant earthquakes represent signals with Ts-Tp > ~6 s, where all 91 earthquakes from the revised National Observatory of Athens (NOA) catalog within ~50 km of the cable starting point (Fig. 1b) are included in the histogram. Vertical lines indicate M2.5+ earthquakes from the revised NOA catalog.

We manually inspect all detections and classify them into three groups: i) local earthquakes (Fig. 4, Fig. 5a–b), ii) distant earthquakes (with $T_S-T_P>\sim6$ s) (Fig. 4, Fig. 5c), and iii) false detections (Fig. 4, Fig. 5d–e). Local earthquakes (5,734), include events within ~50 km of the start of the cable, are identified by coherent signals along the fiber that commonly have clearly visible P- and/or S-wave arrivals (Fig. 5a–b). Smaller-amplitude earthquakes are recognizable primarily from characteristic reverberations between channels 5000–5500 in the submarine section of the cable (Fig. 5b). We inspect some of the weaker amplitude earthquakes with a spectral over-subtraction denoiser (Pascucci et al., 2025) to confirm that the signals correspond to real seismic events (Fig. S4). False detections (684) include non-seismic signals (e.g., boat noise; Fig. 5d), triggers within the coda of larger events where P- and S-wave arrivals are absent or unclear (Fig. 5e), and duplicate entries. In the case of duplicate detections, we retain the earliest detection (typically the P-wave arrival) and classify the latter detection as false. For example, we retain the P-wave arrival in Fig. 5c as the detection of the distant event, while the S-wave arrival is rejected as a false detection. We obtain a false detection rate of approximately 6% (399 out of 6,817 detections), which we consider a conservative overestimate. This is because some cases classified as false detections correspond to S-wave arrivals for which the associated P-wave is also detected, but the S-wave was not automatically

https://doi.org/10.5194/essd-2025-715
Preprint. Discussion started: 13 January 2026

removed during the 3-second de-clustering process. Manual inspection of signals also reveals some missed events, particularly during the most active periods (i.e., after the 8th of August, Fig. S6).

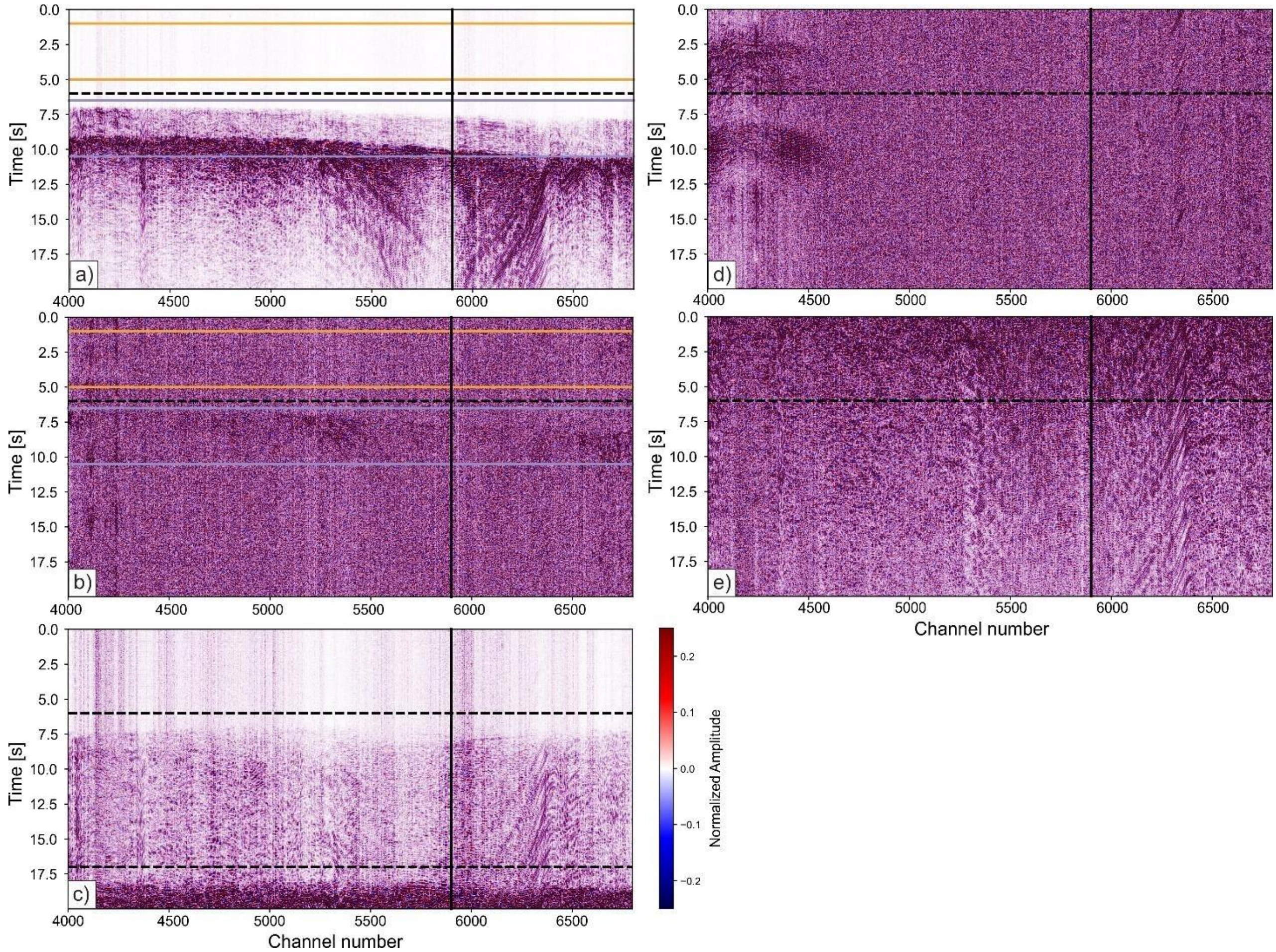

Figure 5. Example types of event detections. (a) M_L 1.2 earthquake, (b) M_L 0.3 earthquake, (c) distant earthquake, (d) false detection, (e) false detection. Panel (d) likely shows a signal from a boat while e) represents a detection within the coda of an earthquake. We obtain two detections in panel (c), where the earlier detection (P-wave arrival) is retained. We declare the second detection from the S-wave arrival as false. Dashed horizontal lines indicate the detection time obtained from HECTOR while the orange and purple lines in panels a-b indicate noise and signal windows (4 seconds), respectively, that are used to calculate the signal-to-noise (SNR) ratios. The detections result from channels 4000-5900, while SNR ratios result from all offshore channels 4000-6800 (signals with the highest SNR, Fig. 2). Fig. S5a-b shows the event in panel (b) before and after the application of a spectral over-subtraction denoiser.

4. Earthquake location and local magnitude estimates.

We initially locate and calculate local magnitudes for high-SNR detected local earthquakes by combining DAS and seismic station data. We calculate SNR on offshore fiber channels (4000-6800) considering a noise window from 1-5 seconds before the detection time and a signal window from 0.5-4.5 seconds after the detection time (Fig. 5). We compute average Root-

https://doi.org/10.5194/essd-2025-715
Preprint. Discussion started: 13 January 2026

Mean-Square (RMS) values for noise and signal on traces bandpass filtered between 5–20 Hz, using a trimmed mean that removes the highest and lowest 10% of values (trim fraction 0.1).

We then calculate SNR as follows:

$$SNR = 20\log_{10}(RMS_{signal}/RMS_{noise}).$$

We consider local earthquakes (following the criteria reported above) with SNR > 15 for hypocentral location and magnitude estimation, resulting in a subset of 297 events from the 5,734 detected local earthquakes. The restrictive SNR threshold reflects the goal of building a high-quality reference catalog of locations and magnitudes. We perform automatic P- and S-wave arrival picking on DAS data using PhaseNet-DAS (Zhu et al., 2023) for each of the 297 earthquakes. We define 20-second windows for PhaseNet-DAS that start 6 seconds before the detection time and end 14 seconds after it (same as in Fig. 5). We note that we convert strain to stain-rates as one of the required pre-processing steps for PhaseNet-DAS and bandpass filter the records between 5-40 Hz. We observe P and S arrivals of good quality despite PhaseNet-DAS being trained on raw strain rate data sampled at 100 Hz (Fig. S7).

To reduce the number of DAS channels for earthquake locations and make it comparable to the number of seismic stations, we split the optical fiber into 12 segments based on azimuthal coverage and number of channels (Fig. 1c). We choose segments based on a clustering algorithm that allows a maximum azimuthal variation of 60°, use an azimuth smoothing window of 50 channels, and a minimum number of 100 channels per fiber segment. We assign median P- and S-wave arrival times that we estimate in a prior step with PhaseNet-DAS applied to the entire fiber to the median channel for each of the 12 segments. Finally, we download waveforms from the seven stations closest to the fiber (Fig. 1, Fig. S3) and manually pick P- and S-wave arrival for each of the 297 earthquakes in Snuffler (Heimann et al., 2017) when data quality permits.

4.1 Earthquake location

We consider events with a P- or an S-wave arrival identified by Phasenet-DAS on at least 10 of the 12 fiber segments and with a clear P- or S-wave arrival at a minimum of 3 seismic stations for earthquake location. The minimum required number of segments and stations assures adequate azimuthal coverage for the events in the cluster offshore northwest of Kefalonia. We compute earthquake locations with NLLoc (Lomax et al., 2000) using arrival times from both DAS and seismic station data and a local 1-D velocity model (Haslinger et al., 1999). We revised the original velocity model by removing the second layer at 0.5 km depth (Vp = 5.47 km/s), maintaining lower velocities from 0 to 2 km depth (Table S1) to reflect the presence of unconsolidated sediments beneath the offshore cable segment. We calculate static phase arrival time residuals at the seismic stations and DAS channels used for location and include them in the final NLLoc run. Incorporating these residuals partially accounts for velocity model heterogeneities and mitigates the limitations of a 1D model. We note, however, that static station corrections are influenced by the spatial distribution of seismicity and are most appropriate for the region with the highest event density for this data set. We successfully locate 284 of the 297 local earthquakes (Fig. 6). Hypocenter

https://doi.org/10.5194/essd-2025-715
Preprint. Discussion started: 13 January 2026

solutions for the remaining events were either recorded at only two seismic stations or lacked a median phase arrival time on at least 10 cable segments, which inhibited robust solutions. We obtain average semi-major and semi-minor axis error ellipse values of 1.5±0.5 and 0.8±0.5 km, respectively, and vertical errors of 1.9±0.7 km (Fig. S8). A total of 280 of the 284 earthquakes have semi-major error ellipse axis values and vertical errors < 5 km (Fig. S8).

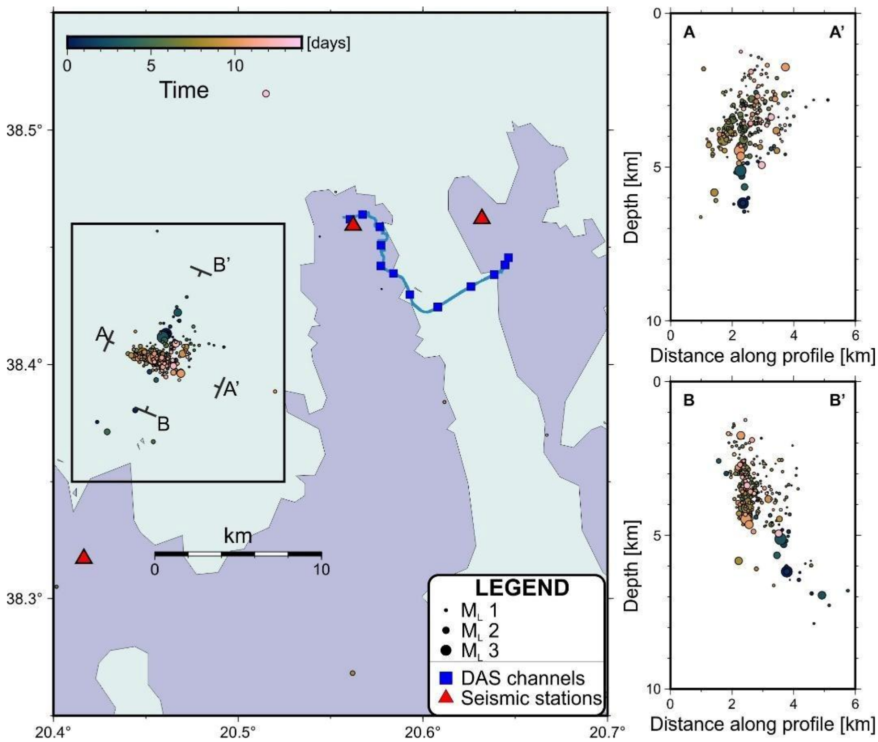

Figure 6. Earthquake locations derived from events with average SNR > 15, estimated along the offshore portion of the optical fiber (channels 4000–6800) by combining P- and S-wave arrival times from DAS and seven nearby seismic station data. Local magnitudes are computed using data from the four seismic stations on Kefalonia and one on Ithaki (shown in Fig. 1). Blue squares indicate the median channel positions for each fiber segment, associated with the corresponding median P- and S-wave arrival times (see Fig. 1 and Section 4). The black box denotes the area shown by the pink box in Fig. 1 and outlines the most seismically active region during the two-week study period. Seismicity cross-sections include events located within 2 km of either side of each profile trace.

4.2 Earthquake magnitude estimate

We estimate local magnitude (M_L) of located earthquakes using seismic station data following the empirical equation of Hutton and Boore (1987). We apply a bandpass filter to the waveforms in the band 2–30 Hz and calculate the maximum amplitude on the two horizontal components at each of the four seismic stations on Kefalonia and the one on Ithaki (Fig. 1). We restrict the magnitude analysis to the four stations with the largest number of picks (FSK, DMLN, ITHC, VLS) and a fifth station ATHR because of its proximity to the cluster of seismicity northwest of Kefalonia (Fig. 1). At each station we consider the maximum amplitude between the two horizontal components for magnitude estimate. Because some events

https://doi.org/10.5194/essd-2025-715
Preprint. Discussion started: 13 January 2026

Open Access Earth System Science Data Discussions

have low amplitudes and are not always clearly visible at five stations, or because some signal windows may contain overlapping earthquakes, we calculate M_L using only the individual station magnitudes that differ by less than $\Delta M = 0.5$ from the average event magnitude estimate. We require at least three station magnitudes with $\Delta M < 0.5$ to assign a final M_L, which is then computed as the average of the retained values. M_L estimates are possible for all 284 earthquakes based on the above quality control requirements, and values range from 0.3 to 3.3. We note that a M_L 3.4 earthquake is not included in the 284 earthquakes. While the earthquake is successfully detected, it fails to meet the quality control criteria because it has a SNR = 5.3. The low SNR results from the fact that its origin time is ~12 seconds after a nearby M_L 3.0 whose coda contaminates the window containing the primary phase arrival of the M_L 3.4. Nevertheless, the final catalog includes the event because it is added during enhancement by cross-correlation and its magnitude is correctly retrieved from the amplitude ratio (details follow in Section 5). A comparison of earthquake magnitudes estimated here and common events in the revised NOA catalog shows a correlation coefficient of R = 0.96 and a near one-to-one relationship, suggesting a strong correlation (Fig. S9).

5. Catalog enhancement using waveform cross-correlation of DAS data

We begin catalog enhancement by using 280 of the 284 located earthquakes as template events. We omit four events from the group of templates that have either a semi-major error ellipse axis and/or a depth error > 5 km. The reason for using the error cutoff is that large location uncertainties may lead to large errors in M_L, and we calculate relative magnitudes during enhancement using the amplitude ratio between templates and target events. We begin by cross-correlating each of the 5,454 detected local earthquakes without a location and a magnitude estimate (target events) with the 280 template events. We keep the initial location, and magnitude estimates for the four events previously excluded based on their larger (> 5 km) hypocentral error. Each target event is then assigned the location of the corresponding template event with highest similarity. We downsample the continuous waveform data to 50 Hz for the cross-correlation calculation and use the same offshore channels (4000–5900) that are used for detection (Fig. 7). All traces are bandpass filtered between 5–20 Hz before computing channel-based Cross-Correlation Coefficients (CCC) for 4-second time windows that begin 0.5 seconds after the detection time (Fig. 7-8).

We observe that CCC varies across channels (Fig. 7a, Fig. S10a) and that higher CCC values are associated with channels with higher SNR (Fig. 7c–d, Fig. S8c-d). To account for varying CCC with SNR, we apply an SNR criterion before averaging the CCC values of individual channels. We then compute the average CCC between event pairs using the Fisher mean (Fisher, 1921; Silver and Dunlap, 1987), after excluding 67% of the channels (i.e., 1,273 channels) with the lowest SNR (Fig. 7e, Fig. S10e). The SNR estimation uses the 4-second signal and noise windows noted above (Fig. 5), and the cutoff threshold is determined based on the lowest-amplitude earthquake in each event pair (Fig. 7b).

https://doi.org/10.5194/essd-2025-715
Preprint. Discussion started: 13 January 2026

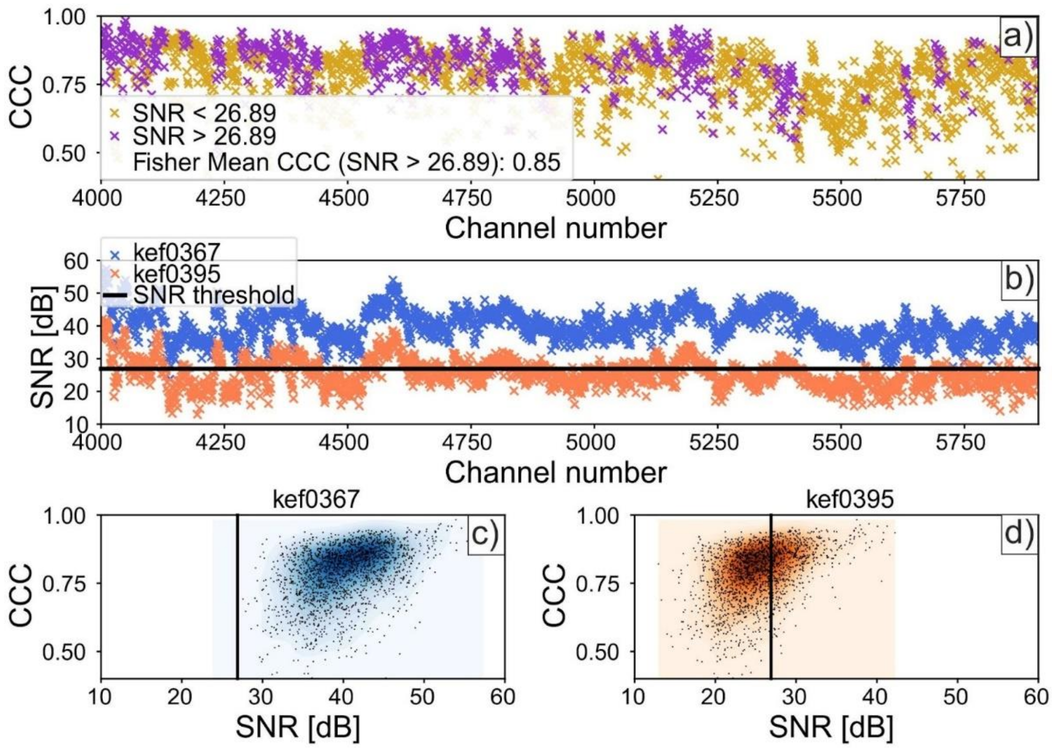

Figure 7. Waveform Cross-Correlation Coefficient (CCC) analysis for event pair *kef0367* (M_L 1.7) and *kef0395* (M_L 1.0). (a) CCC of individual DAS traces from channels 4000-5900. (a) Purple and gold symbols are CCC values above and below a SNR threshold calculated from the smaller amplitude event in the pair (see text and description in panel b of this figure). (b) Signal-to-noise ratio (SNR) of each event in the pair. SNR (in dB) is calculated as the ratio between the root-mean-square of the signal in 4-second windows starting 0.5 s after the detection time and noise windows of the same length starting 5 s before the detection time (refer to Fig. 3a for SNR windows). The thick horizontal black line marks the minimum SNR threshold required for the CCC calculation, which is defined by the lower-amplitude event. The threshold corresponds to the cutoff of the top 33% of channels with the highest SNR. (c–d) CCC versus SNR for events kef0367 and kef0395. The vertical black line indicates the minimum SNR threshold. Average cross-correlation coefficient of the event pair is 0.85, estimated as the Fisher mean of the individual CCC values. Traces are bandpass-filtered 5-20 Hz. The correlation between SNR and CCC at individual traces is even clearer when showing CCC values over the entire cable (Fig. S10).

Before selecting the minimum CCC value for associating a target event with a template and proceeding with relative magnitude calculations, we first examine the expected decay of CCC with inter-event distance (Menke et al., 1990). We do so by cross-correlating all template events with one another (excluding the four events noted above with larger hypocentral uncertainties) following the procedure outlined earlier in this section. We restrict the analysis to template earthquakes since we know their locations. Because only absolute locations are available, our inter-event distance estimates for given CCC values should be considered conservative.

As expected, inter-event distance increases systematically with decreasing CCC (Fig. S11). For instance, we obtain a median inter-event distance of < 2 km and a 95th percentile of ~5 km for a pair with a CCC of 0.52 (Fig. S11). At 15 km distance, this corresponds to a magnitude error of 0.06 for a 2 km interevent separation and 0.15 for a 5 km interevent separation. At

https://doi.org/10.5194/essd-2025-715
Preprint. Discussion started: 13 January 2026

10 km distance, the corresponding errors are 0.05 and 0.2, respectively. In this study, we present results using a conservative CCC threshold of 0.52 that allows us to associate 2,496 target events to template events. We make all event pair CCC values available so that catalog users can test the effects of using different CCC thresholds to associate target and template events. In Figure 8, we show examples of target-template pairs exceeding the CCC threshold. We observe that nearly all target events (>97-98%) are associated with template events from the cluster northwest of Kefalonia (Fig. S12).

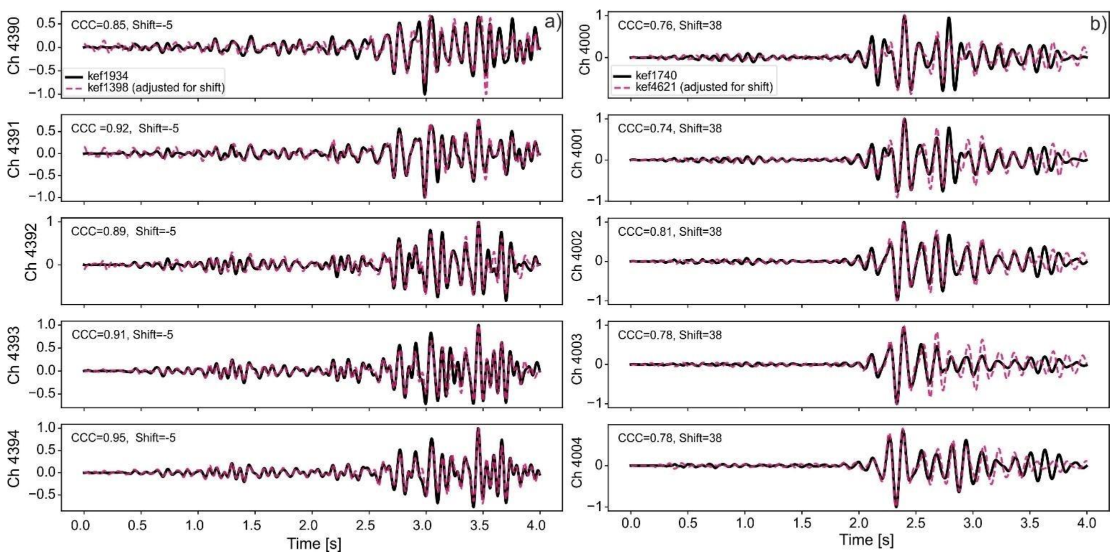

Figure 8. Event pair (template-target) cross-correlation. Black traces are template events with location, and a M_L estimates, while in magenta it is the target event with no (initial) location or magnitude estimate. (a) Event pair kef1934 (M_L 1.2) and kef1398 (M_L 0.2) with average CCC of 0.93. (b) Event pair kef1740 (M_L 0.6) and kef4621 (M_L 0.0) with an average CCC of 0.58. Traces are bandpass filtered at 5-20 Hz and normalized to make waveforms comparable. CCC is calculated in 4-second windows starting 0.5 seconds after the detection time. CCC at a given channel and time shift (in samples) are indicated for each subpanel.

Before calculating amplitude ratios for the determination of relative magnitudes, we first inspect whether we can correctly retrieve the magnitudes of template events using amplitude ratios, where template M_L estimates originate from seismic stations. We associate each template event with its most similar template and recalculate the magnitude from the amplitude ratio of bandpassed traces (5-20 Hz) on channels 4000-5900. We consider the average of the maximum amplitudes of all traces after removing the highest and lowest 10% values (i.e., trimmed mean) for event pairs with CCC values > 0.52. We calculate relative magnitudes as follows:

$$M_{target}=M_{template} + \log10(A_{target}/A_{template})$$

where M is the magnitude and A is the average of the maximum amplitude.

https://doi.org/10.5194/essd-2025-715
Preprint. Discussion started: 13 January 2026

Open Access Earth System Science Data Discussions

We find strong agreement between initial M_L and relative M_L estimates across the full magnitude range, indicated by a coefficient of determination $R^2 = 0.92$ and a best-fitting line slope of nearly 1:1. Thus, we proceed with the calculations of relative magnitudes for all target events with a minimum CCC > 0.52 (2,496 events) with respect to their template events.

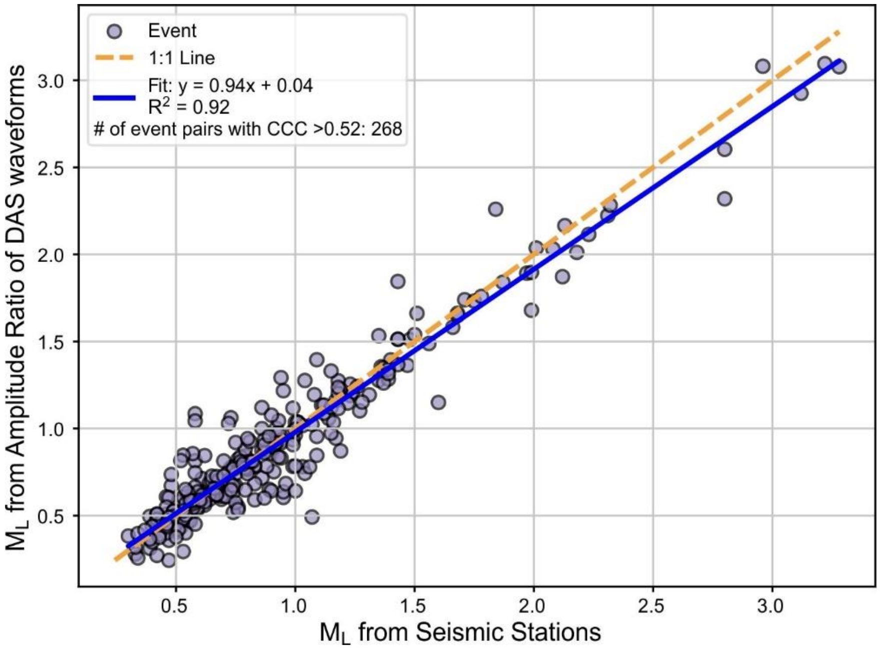

Figure 9. M_L from seismic stations versus relative M_L derived from DAS data. The analysis includes all located earthquakes (i.e. templates) with semi-major error ellipse axes and vertical error < 5 km (280 events). Relative M_L for each template event is obtained from the mean amplitude ratio with respect to the most similar event using bandpass filtered waveforms (5-20 Hz). Average amplitude ratios are calculated using event pairs with a Cross-Correlation Coefficient (CCC) > 0.52 (268 of the 280 template events) on channels 4000–5900 using a trimmed mean that exclude the highest and lowest 10% of values.

Adding relative magnitude estimates to the 284 events with M_L calculated from seismic stations leads to 2,780 magnitude estimates (48.5% of the local earthquakes). We observe that 2,718 earthquakes with a magnitude estimate (97.7%) are located offshore northwest of Kefalonia and are mostly clustered in space (Fig. 1, Fig. 5, Fig. S12). The remaining events are scattered within the study region (Fig. S12), with a few clusters located along the Strait of Ithaki. Figure S11 shows the distribution of all events detected and located in this study with a magnitude estimate. There are 11 events in common with the revised NOA catalog that are not included in our catalog of 284 events, despite being successfully detected. Nine of the eleven events common to the NOA catalog are omitted because of their average SNR at offshore DAS channels being <15 (nine events), and they were therefore not considered for initial location (Section 4.1). The last two of the eleven events are omitted because we observe T_S-T_P > 6 seconds at offshore DAS channels. The fact that we detect but do not locate a few earthquakes included in the revised NOA catalog reflects our focus on detecting and locating seismicity in the highly active region offshore northwest of Kefalonia. By considering events within the active region northwest of Kefalonia (Fig. 1, Fig. 5, Fig. S12), we observe a ~37-fold increase in the number of events with a magnitude estimate relative to the revised NOA catalog (Fig. 10). All events in our catalog down to M_L 2.4 are common to the NOA catalog (Fig. 10a), while the number of

https://doi.org/10.5194/essd-2025-715
Preprint. Discussion started: 13 January 2026

events from this study significantly increases at lower magnitudes (Fig. 10). Specifically, we estimate a magnitude of completeness of M_c = -0.5 using a maximum curvature and Goodness-of-Fit Test (Wiemer and Wyss, 2000) and a b-value = 0.85±0.02 based on the maximum likelihood estimate (Aki, 1965) (Fig. 10a). The enhanced earthquake catalog shows interevent times as short as 3 seconds (the minimum allowed inter-event time from de-clustering) and average inter-event times for 100-event windows down to 30 seconds.

https://doi.org/10.5194/essd-2025-715
Preprint. Discussion started: 13 January 2026

Open Access Earth System Science Data Discussions

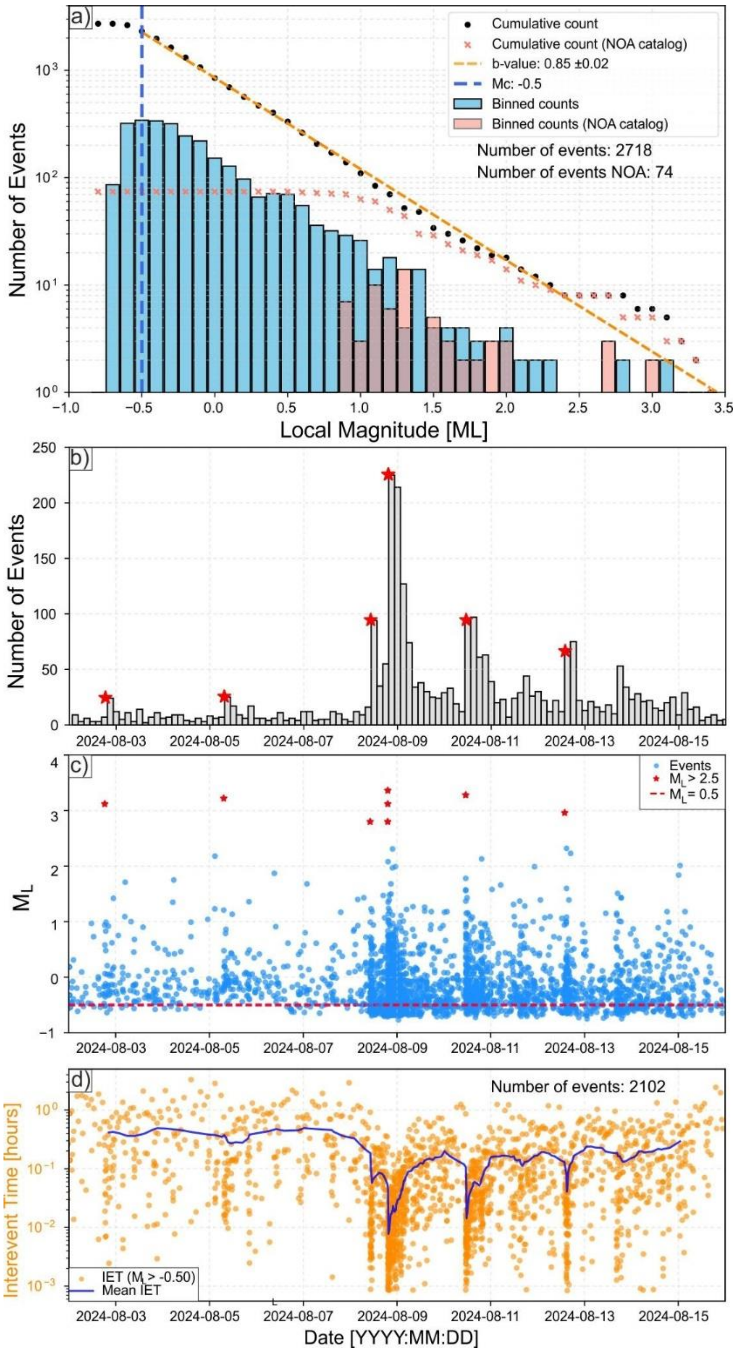

Figure 10. Time–space–magnitude distribution of seismicity in the region 38.35–38.46°N, 20.41–20.525°E (black box in Fig. 1 and Fig. 6). (a) Frequency–magnitude distribution of events from this study compared with events from the National Observatory of Athens for the same period and region. The b-value is estimated using Maximum Likelihood (Aki, 1965), and the magnitude of completeness (M_c) using the Goodness-of-Fit Test and Maximum Curvature method (Weimer and Wyss, 2000). (b) Number of events over time (3-hour bins). Red stars indicate M_L > 2.5 earthquakes. (c) Event magnitudes versus time for individual events. (d) Inter-event times (100-event sliding windows with 90% overlap) between successive events with M_L > M_c plotted against time.

https://doi.org/10.5194/essd-2025-715
Preprint. Discussion started: 13 January 2026

6. Discussion

The main goal of this work is to integrate data from DAS and conventional seismic networks to construct a high-resolution earthquake catalog. One notable feature of this dataset is the exceptionally high seismicity rate within 10–15 km of the optical fiber, which at times exceeds 100 events per hour (Fig. 1, Fig. 6). Although other open-access DAS datasets also contain high event rates, most of them were acquired in boreholes and target induced seismicity (the FORGE dataset, Porras et al., 2024), rather than natural earthquake sequences.

Concerning our dataset, the highest seismicity rates occur offshore in a cluster northwest of Kefalonia with a ~5 km radius where azimuthal coverage from land stations is limited (Fig. 1, Fig. 6). The intense seismic activity combined with sparse station geometry are challenging for the monitoring of active seismic sequences (Grigoli et al., 2021; Karastathis et al., 2015). This work shows that combining DAS and seismic station data can make it possible to overcome some of the challenges associated with observing offshore earthquakes: using DAS channels for dense wavefield sampling and earthquake detection, combining DAS and seismic station data for determining hypocenter locations, and using seismic stations for amplitude calibration and magnitude estimation.

The enhanced catalog presented here exhibits high temporal resolution, with inter-event times as short as three seconds and a completeness magnitude of Mc = -0.5. It captures evolving statistical features of the seismic sequence, including a transition from more Poisson-like inter-event time distribution to densely clustered activity associated with mainshock–aftershock activity (Figure 10c). The catalog also reveals notable changes in aftershock productivity. For instance, two M > 3 earthquakes before 8 August 2024 were not followed by clear aftershock activity, whereas similar-sized and smaller events after that date produced pronounced aftershock sequences (Figure 10b-c). After 8 August, we observe a systematic relation between mainshock magnitude and aftershock inter-event times, with larger mainshocks followed by shorter aftershock inter-event times (Figure 10d). The distribution of the seismicity highlights a nearly vertical WNW-ESE striking fault (Fig. 6), which is consistent with the geometry observed by Anagnostou et al. (2025), who used 3-month data between the end of February and the end of April 2025. These observations underscore the high spatial and temporal resolution of the catalog that we will discuss in a detailed analysis of the space–time–magnitude patterns that will be addressed in a separate study.

The amphibious nature of the telecommunication cable introduces additional features of shallow crustal structure that are worth investigating, such as the strong signal amplification observed along the marine segment and its potential influence on magnitude determination when using only DAS data.

6.1 Distorted waveforms

The close proximity of the cable and the large magnitudes of the sequence also led to distorted waveforms on many channels after the S-wave arrival for earthquakes with M_L > ~2. The distortion is mostly limited to offshore channels but can also appear on onshore channels for events with M_L > ~2.8. This distortion is likely related to cycle-skipping issues in DAS caused by dynamic range limitations (Katakami et al., 2024). However, determining the exact cause is challenging because

https://doi.org/10.5194/essd-2025-715
Preprint. Discussion started: 13 January 2026

Open Access Earth System Science Data Discussions

the data were decimated by a factor of 20 before storage (from 5000 Hz to 250 Hz), eliminating higher-frequency energy above 125 Hz. With our settings, the maximum change measurable between consecutive samples is ~0.033 με (±π). While the QuantX instrument can measure larger signal amplitudes, it cannot track phase changes exceeding ±π between consecutive samples. Nevertheless, the observed distortion of the signals, likely due to cycle-skipping, did not affect our analysis: maximum earthquake amplitudes are correctly measured (Fig. 9), and waveform shapes remain undistorted after bandpassing earthquakes in our frequency range of interest (Fig. 11).

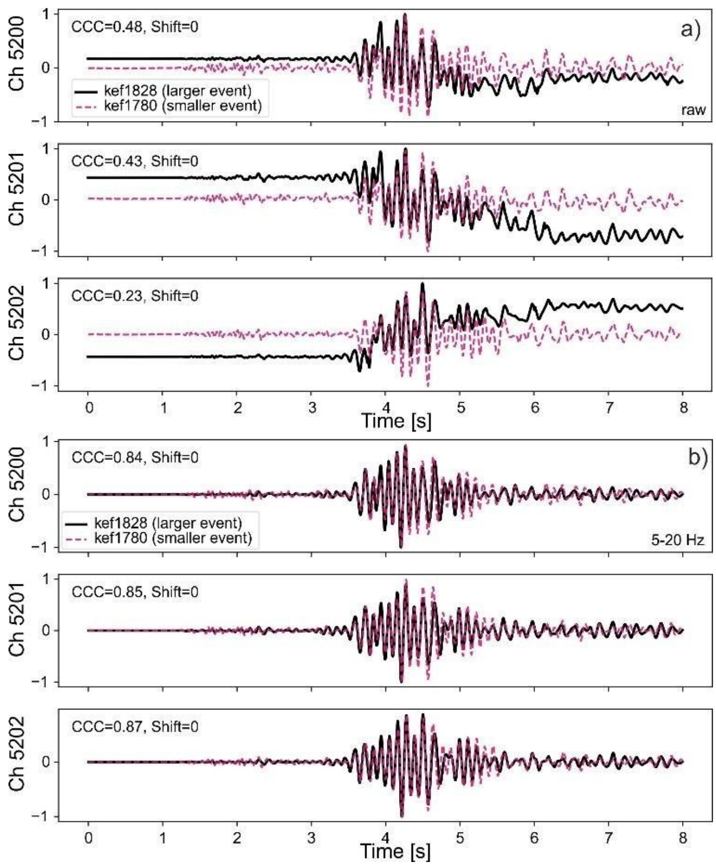

Figure 11. Waveforms of similar events (average CCC = 0.7 from DAS), one of which is affected by cycle skipping. The M_L 2.8 event kef1828 (black) shows waveform distortion at the S-wave arrival, while the M_L 1.4 event kef1780 (violet) does not. (a) Raw waveforms. (b) Band-pass filtered waveforms (5–20 Hz). Hypocentral locations: kef1780 – 38.4018°N, 20.4502°E, depth 3.41 km; kef1828 – 38.4018°N, 20.4547°E, depth 3.76 km. Note the high waveform similarity after filtering the traces. The events show an average CCC of 0.7 at seismic stations (Fig. S13)

7. Applications

The dataset released in this work offers a wide range of applications. The exceptionally high seismicity rate, with inter-event times as short as three seconds, creates an ideal testbed for developing and evaluating advanced detection and location methods tailored to DAS data. To support such efforts, we provide a detailed, manually verified event catalog that serves as

https://doi.org/10.5194/essd-2025-715
Preprint. Discussion started: 13 January 2026

Open Access Earth System Science Data Discussions

a reliable reference. In addition, the inclusion of very small-amplitude signals, some with magnitude estimates and others without, offers a valuable opportunity to design and test denoising methods (e.g., Fig. S5).

The integration of the DAS array within an open-access seismic network makes this dataset a controlled environment for evaluating DAS-enhanced seismic event-location performance and for the development of new hybrid location techniques. Furthermore, DAS recordings acquired on the ocean floor may exhibit a higher signal-to-noise ratio compared to more distant land-based seismometers. This setting also allows testing of various strategies to mitigate biases arising from the large difference in the number of sensors between the DAS cable and the traditional network, such as automatic DAS channel selection. Finally, the dataset provides valuable opportunities for machine learning applications. With nearly 6,000 recorded events, it can be used to train new models or to investigate transfer learning of existing ones.

8. Data & code Availability

Continuous DAS data waveforms are available from: https://www.geophysik.ruhr-uni-bochum.de/~marco/ReSeed/

Codes to read and plot the events (or detections) recorded along the optical fiber, earthquake catalogs, event pairs cross-correlation coefficients, cable geometry, and PhaseNet-DAS picks are available from: https://gitlab.ruhr-uni-bochum.de/bocchgxw/das-kefalonia/-/tree/7a1933f67475119fb281f4efb43f0370686e00b8/

We use PhaseNet-DAS (Zhu et al., 2023) for phase picking on DAS data, which is available from https://ai4eps.github.io/EQNet/phasenet_das/

We use HECTOR (Porras et al., 2024) for event detection on DAS data, which is available from https://github.com/juanucr/HECTOR/tree/main

We use Snuffler, available through Pyrocko, for manual picking of seismic waveforms (Heimann et al., 2017)

We use Obspy for processing of seismic station waveforms (Beyreuther et al., 2010)

We create figures using Matplotlib (Hunter, 2007) and GMT (Wessel et al., 2019).

Seismic station waveforms can be downloaded through the NOA EIDA node (https://eida.gein.noa.gr/), networks HL, HP, HA, HT.

9. Conclusions

In this study, we use DAS recordings together with permanent seismic stations from the HUSN to construct a high-resolution earthquake catalog for Kefalonia Island between 2-15 August 2024. Applying a semblance-based detector enables identification of more than 5,700 earthquakes within a ~50 km radius of the starting point of the optical fiber. Combining DAS and seismic data analysis and waveform cross-correlation enables location and magnitude estimates of 2,780 events, of which 2,718 concentrate in an active cluster offshore northwest of Kefalonia. The catalog shows very high seismicity rates with peaks in earthquake rates that exceed 100 events per hour, and average inter-event times as short as 30 seconds derived

https://doi.org/10.5194/essd-2025-715
Preprint. Discussion started: 13 January 2026

from 100-event windows. The short inter-event times and a magnitude of completeness (M_c) of -0.5 enable a detailed spatiotemporal analysis of the seismicity.

A comparison of the catalog produced here and the revised earthquake catalog of NOA for the active cluster northwest of Kefalonia shows the same number of events down to M_L 2.4, and a factor of ~37 increase in smaller events for the DAS-seismic-data catalog. The detailed catalog underscores the benefit of using DAS to strengthen seismic monitoring in regions where station coverage is limited and seismicity is intense.

Finally, the main objective of this work is to provide the community with a data set that includes an earthquake catalog, a comprehensive detection list, and two weeks of continuous DAS recordings that can be used to benchmark methodological developments. Such developments may include testing new DAS processing techniques, integrating DAS with standard seismic networks for enhanced monitoring of seismic sequences, and detailed studies of earthquake clustering and processes driving complex seismicity, among many others that we anticipate will be conceived by the community.

Author contribution

G.M.B. Conceptualization, Writing - original draft, Writing - review and editing, Methodology, Visualization, Formal analysis, Data curation, Investigation. E.B. Conceptualization, Writing - review and editing, Methodology, Formal Analysis. M.P.R. Formal analysis, Data curation, Investigation. S.G. Conceptualization, Formal Analysis. G.P. Conceptualization, Formal Analysis. F.G. Conceptualization, Methodology, Writing - review and editing. E. B. Writing - review and editing. E. S. Writing - review and editing. R.M.H. Funding acquisition, Conceptualization, Writing - review and editing, Investigation.

Competing interests

The authors declare that they have no competing interests.

Disclaimer.

The authors decline responsibility for any possible errors in the dataset that could lead to erroneous evaluations.

Acknowledgements

The authors would like to thank the student assistants D. Drier and M. Roßbach for helping with the location of the DAS channels and with manual picking of events at seismic stations. The authors also thank M. Bagagli for helping with manual inspection of the initial list of detections. The authors would like to thank Dionisis Alisandratos for his patience and help during the set-up of the DAS experiment, and OTE Greece for providing access to the optical fiber. G.M.B., M.P.R., and R.M.H., would like to thank Roger Crickmore (Luna Innovations) for the helpful discussion on cycle skipping in DAS.

Financial support

G.M.B and R.M.H. acknowledge the financial support of the Volkswagen Stiftung.

References

Aki, K.: Maximum likelihood estimate of b in the formula log N= a-bM and its confidence limits, Bull. Earthq. Res. Inst., Tokyo Univ., 43, 237–239, 1965.

Anagnostou, V., Papadimitriou, E., Karakostas, V., and Bäck, T.: Investigating the 2024 Swarm–Like Activity Offshore Kefalonia Island, Aided by Machine Learning Algorithms, Pure Appl. Geophys., 1–31, https://doi.org/10.1007/S00024-025-03766-3/FIGURES/8, 2025.

Basili, R., Danciu, L., Beauval, C., Sesetyan, K., Vilanova, S. P., Adamia, S., Arroucau, P., Atanackov, J., Baize, S., Canora, C., Caputo, R., Carafa, M. M. C., Cushing, E. M., Custódio, S., Demircioglu Tumsa, M. B., Duarte, J. C., Ganas, A., García-Mayordomo, J., Gómez De La Peña, L., Gràcia, E., Jamšek Rupnik, P., Jomard, H., Kastelic, V., Maesano, F. E., Martín-Banda, R., Martínez-Loriente, S., Neres, M., Perea, H., Šket Motnikar, B., Tiberti, M. M., Tsereteli, N., Tsironi, V., Vallone, R., Vanneste, K., Zupančič, P., and Giardini, D.: The European Fault-Source Model 2020 (EFSM20): geologic input data for the European Seismic Hazard Model 2020, Nat. Hazards Earth Syst. Sci., 24, 3945–3976, https://doi.org/10.5194/NHESS-24-3945-2024, 2024.

Beyreuther, M., Barsch, R., Krischer, L., Megies, T., Behr, Y., and Wassermann, J.: ObsPy: A Python Toolbox for Seismology, Seismol. Res. Lett., 81, 530–533, https://doi.org/10.1785/GSSRL.81.3.530, 2010.

Biondi, E., Zhu, W., Li, J., Williams, E. F., and Zhan, Z.: An upper-crust lid over the Long Valley magma chamber, Sci. Adv., 9, https://doi.org/10.1126/SCIADV.ADI9878, 2023a.

Biondi, E., Wang, X., Williams, E. F., and Zhan, Z.: Geolocalization of Large-Scale DAS Channels Using a GPS-Tracked Moving Vehicle, Seismol. Res. Lett., 94, 318–330, https://doi.org/10.1785/0220220169, 2023b.

Bocchini, G. M., Brüstle, A., Becker, D., Meier, T., van Keken, P. E., Ruscic, M., Papadopoulos, G. A., Rische, M., and Friederich, W.: Tearing, segmentation, and backstepping of subduction in the Aegean: New insights from seismicity, Tectonophysics, 734–735, 96–118, https://doi.org/10.1016/j.tecto.2018.04.002, 2018.

Currenti, G., Allegra, M., Cannavò, F., Jousset, P., Prestifilippo, M., Napoli, R., Sciotto, M., Di Grazia, G., Privitera, E., Palazzo, S., and Krawczyk, C.: Distributed dynamic strain sensing of very long period and long period events on telecom fiber-optic cables at Vulcano, Italy, Sci. Rep., 13, 1–17, https://doi.org/10.1038/S41598-023-31779-2, 2023.

Feigl, K., Reinisch, E., Patterson, J., Jreij, S., Parker, L., Nayak, A., Zeng, X., Cardiff, M., Lord, N., Fratta, D., Thurber, C., Wang, H., Robertson, M., Coleman, T., Miller, D., Spielman, P., Akerley, J., Kreemer, C., Morency, C., Matzel, E., Trainor-Guitton, W., and Davatzes, N.: PoroTomo Natural Laboratory Horizontal and Vertical Distributed Acoustic Sensing Data. [Data set], https://doi.org/10.15121/1778858, 2016.

Fisher, R. A.: On the "Probable Error" of a Coefficient of Correlation Deduced from a Small Sample., Metron, 1, 3–32, 1921.

Glubokovskikh, S., Shashkin, P., Shapiro, S., Gurevich, B., and Pevzner, R.: Multiwell Fiber Optic Sensing Reveals Effects of CO2 Flow on Triggered Seismicity, Seismol. Res. Lett., 94, 2215–2230, https://doi.org/10.1785/0220230025, 2023.

Gräff, D., Lipovsky, B. P., Vieli, A., Dachauer, A., Jackson, R., Farinotti, D., Schmale, J., Ampuero, J. P., Berg, E., Dannowski, A., Kneib-Walter, A., Köpfli, M., Kopp, H., van der Loo, E., Mata Flores, D., Mercerat, D., Moser, R., Sladen, A., Walter, F., Wasser, D., Welty, E., Wetter, S., and Williams, E. F.: Calving-driven fjord dynamics resolved by seafloor fibre sensing, Nature, 644, 404–412, https://doi.org/10.1038/S41586-025-09347-7, 2025.

Grigoli, F., Ellsworth, W. L., Zhang, M., Mousavi, M., Cesca, S., Satriano, C., Beroza, G. C., and Wiemer, S.: Relative earthquake location procedure for clustered seismicity with a single station, Geophys. J. Int., 225, 608–626, https://doi.org/10.1093/GJI/GGAA607, 2021.

HA: University of Athens, Seismological Laboratory [Data set], https://doi.org/10.7914/SN/HA, 2008.

Haslinger, F., Kissling, E., Ansorge, J., Hatzfeld, D., Papadimitriou, E., Karakostas, V., Makropoulos, K., Kahle, H. G., and Peter, Y.: 3D crustal structure from local earthquake tomography around the Gulf of Arta (Ionian region, NW Greece), Tectonophysics, 304, 201–218, https://doi.org/10.1016/S0040-1951(98)00298-4, 1999.

Heimann, S., Kriegerowski, M., Isken, M., Cesca, S., Daout, S., Grigoli, F., Juretzek, C., Megies, T., Nooshiri, N., Steinberg, A., Sudhaus, H., Vasyura-Bathke, H., Willey, T., and Dahm, T.: Pyrocko - An open-source seismology toolbox and library, https://doi.org/10.5880/GFZ.2.1.2017.001, 2017.

HL: National Observatory of Athens Seismic Network [Data set], https://doi.org/10.7914/SN/HL, 1975.

HP: University of Patras, Seismological Laboratory [Data set], https://doi.org/10.7914/SN/HP, 2000.

HT: Aristotle University of Thessaloniki Seismological Network [Data set], https://doi.org/10.7914/SN/HT, 1981.

Hunter, J. D.: Matplotlib: A 2D graphics environment, Comput. Sci. Eng., 9, 90–95, https://doi.org/10.1109/MCSE.2007.55, 2007.

Hutton, L. K. and Boore, D. M.: The ML scale in Southern California, Bull. Seismol. Soc. Am., 77, 2074–2094, https://doi.org/10.1785/BSSA0770062074, 1987.

Jousset, P., Currenti, G., Schwarz, B., Chalari, A., Tilmann, F., Reinsch, T., Zuccarello, L., Privitera, E., and Krawczyk, C. M.: Fibre optic distributed acoustic sensing of volcanic events, Nat. Commun., 13, 1–16, https://doi.org/10.1038/S41467-022-29184-w, 2022.

Karastathis, V. K., Mouzakiotis, E., Ganas, A., and Papadopoulos, G. A.: High-precision relocation of seismic sequences above a dipping Moho: the case of the January-February 2014 seismic sequence on Cephalonia island (Greece), Solid Earth, 6, 173, 2015.

https://doi.org/10.5194/essd-2025-715
Preprint. Discussion started: 13 January 2026

Katakami, S., Noda, S., Korenaga, M., Araki, E., Takahashi, N., and Iwata, N.: Potential of Earthquake Strong Motion Observation Utilizing a Linear Estimation Method for Phase Cycle Skipping in Distributed Acoustic Sensing, J. Geophys. Res. Solid Earth, 129, e2023JB027327, https://doi.org/10.1029/2023JB027327, 2024.

Lellouch, A., Schultz, R., Lindsey, N. J., Biondi, B. L., and Ellsworth, W. L.: Low-Magnitude Seismicity With a Downhole Distributed Acoustic Sensing Array—Examples From the FORGE Geothermal Experiment, J. Geophys. Res. Solid Earth, 126, e2020JB020462, https://doi.org/10.1029/2020JB020462, 2021.

Li, J., Zhu, W., Biondi, E., and Zhan, Z.: Earthquake focal mechanisms with distributed acoustic sensing, Nat. Commun., 14, 1–9, https://doi.org/10.1038/S41467-023-39639-3, 2023.

Li, J., Biondi, E., Heimisson, E. R., Puel, S., Zhai, Q., Zhang, S., Hjörleifsdóttir, V., Wei, X., Bird, E., Klesh, A., Kamalov, V., Gunnarsson, T., Geirsson, H., and Zhan, Z.: Minute-scale dynamics of recurrent dike intrusions in Iceland with fiber-optic geodesy, Science (80-.)., 388, 1189–1193, https://doi.org/DOI: 10.1126/science.adu0225, 2025.

Lindsey, N. J., Martin, E. R., Dreger, D. S., Freifeld, B., Cole, S., James, S. R., Biondi, B. L., and Ajo-Franklin, J. B.: Fiber-Optic Network Observations of Earthquake Wavefields, Geophys. Res. Lett., 44, 11,792-11,799, https://doi.org/10.1002/2017GL075722, 2017.

Lior, I., Sladen, A., Rivet, D., Ampuero, J. P., Hello, Y., Becerril, C., Martins, H. F., Lamare, P., Jestin, C., Tsagkli, S., and Markou, C.: On the Detection Capabilities of Underwater Distributed Acoustic Sensing, J. Geophys. Res. Solid Earth, 126, e2020JB020925, https://doi.org/10.1029/2020JB020925, 2021a.

Lior, I., Sladen, A., Mercerat, D., Ampuero, J. P., Rivet, D., and Sambolian, S.: Strain to ground motion conversion of distributed acoustic sensing data for earthquake magnitude and stress drop determination, Solid Earth, 12, 1421–1442, https://doi.org/10.5194/SE-12-1421-2021, 2021b.

Lomax, A., Virieux, J., Volant, P., and Berge-Thierry, C.: Probabilistic earthquake location in 3D and layered models, in: Advances in seismic event location, edited by: Thurber, C.H. and Rabinowitz, N., Springer, Dordrecht, Kluwer, Amsterdam, 101–134, https://doi.org/https://doi.org/10.1007/978-94-015-9536-0_5, 2000.

Louvari, E., Kiratzi, A. A., and Papazachos, B. C.: The Cephalonia Transform Fault and its extension to western Lefkada Island (Greece), Tectonophysics, 308, 223–236, https://doi.org/10.1016/S0040-1951(99)00078-5, 1999.

Menke, W., Lerner-Lam, A. L., Dubendorff, B., and Pacheco, J.: Polarization and coherence of 5 to 30 Hz seismic wave fields at a hard-rock site and their relevance to velocity heterogeneities in the crust, Bull. Seismol. Soc. Am., 80, 430–449, https://doi.org/10.1785/BSSA0800020430, 1990.

Pankow, K.: Utah FORGE: Distributed Acoustic Sensing Data 2022. [Data set], https://gdr.openei.org/submissions/1393, 2022.

Papadimitriou, E. E.: Mode of Strong Earthquake Recurrence in the Central Ionian Islands (Greece): Possible Triggering due to Coulomb Stress Changes Generated by the Occurrence of Previous Strong Shocks, Bull. Seismol. Soc. Am., 92, 3293–3308, https://doi.org/10.1785/0120000290, 2002.

Pascucci, G., Gaviano, S., Pozzoli, A., Grigoli, F: Signal Enhancement of Distributed Acoustic Sensing data using a Spectral

Subtraction-based Approach. Seismol. Res. Lett., (in-press)

Pérouse, E., Chamot-Rooke, N., Rabaute, A., Briole, P., Jouanne, F., Georgiev, I., and Dimitrov, D.: Bridging onshore and offshore present-day kinematics of central and eastern Mediterranean: Implications for crustal dynamics and mantle flow, Geochemistry, Geophys. Geosystems, https://doi.org/10.1029/2012GC004289, 2012.

Porras, J., Pecci, D., Bocchini, G. M., Gaviano, S., De Solda, M., Tuinstra, K., Lanza, F., Tognarelli, A., Stucchi, E., and Grigoli, F.: A semblance-based microseismic event detector for DAS data, Geophys. J. Int., 236, 1716–1727, https://doi.org/10.1093/GJI/GGAE016, 2024.

Royden, L. H. and Papanikolaou, D. J.: Slab segmentation and late Cenozoic disruption of the Hellenic arc, Geochemistry, Geophys. Geosystems, 12, 1–24, https://doi.org/10.1029/2010GC003280, 2011.

Scordilis, E. M., Karakaisis, G. F., Karacostas, B. G., Panagiotopoulos, D. G., Comninakis, P. E., and Papazachos, B. C.: Evidence for transform faulting in the Ionian sea: The Cephalonia island earthquake sequence of 1983, Pure Appl. Geophys., https://doi.org/10.1007/BF00880738, 1985.

Seguí, A., Ugalde, A., Fichtner, A., Ventosa, S., Morros, J. R., Seguí, A., Ugalde, A., Fichtner, A., Ventosa, S., and Morros, R.: DASPack: Controlled Data Compression for Distributed Acoustic Sensing, Geophys. J. Int., https://doi.org/10.1093/GJI/GGAF397, 2025.

Silver, N. C. and Dunlap, W. P.: Averaging Correlation Coefficients: Should Fisher's z Transformation Be Used?, J. Appl. Psychol., 72, 146–148, https://doi.org/10.1037/0021-9010.72.1.146, 1987.

Spica, Z. J., Ajo-Franklin, J., Beroza, G. C., Biondi, B., Cheng, F., Gaite, B., Luo, B., Martin, E., Shen, J., Thurber, C., Viens, L., Wang, H., Wuestefeld, A., Xiao, H., and Zhu, T.: PubDAS: A PUBlic Distributed Acoustic Sensing Datasets Repository for Geosciences, Seismol. Res. Lett., 94, 983–998, https://doi.org/10.1785/0220220279, 2023.

Wessel, P., Luis, J. F., Uieda, L., Scharroo, R., Wobbe, F., Smith, W. H. F., and Tian, D.: The Generic Mapping Tools Version 6, Geochemistry, Geophys. Geosystems, 20, 5556–5564, https://doi.org/10.1029/2019GC008515, 2019.

Wiemer, S. and Wyss, M.: Minimum magnitude of completeness in earthquake catalogs: Examples from Alaska, the Western United States, and Japan, Bull. Seismol. Soc. Am., 90, 859–869, https://doi.org/10.1785/0119990114, 2000.

Wuestefeld, A., Spica, Z. J., Aderhold, K., Huang, H. H., Ma, K. F., Lai, V. H., Miller, M., Urmantseva, L., Zapf, D., Bowden, D. C., Edme, P., Kiers, T., Rinaldi, A. P., Tuinstra, K., Jestin, C., Diaz-Meza, S., Jousset, P., Wollin, C., Ugalde, A., Barajas, S. R., Gaite, B., Currenti, G., Prestifilippo, M., Araki, E., Tonegawa, T., de Ridder, S., Nowacki, A., Lindner, F., Schoenball, M., Wetter, C., Zhu, H. H., Baird, A. F., Rørstadbotnen, R. A., Ajo-Franklin, J., Ma, Y., Abbott, R. E., Hodgkinson, K. M., Porritt, R. W., Stanciu, C., Podrasky, A., Hill, D., Biondi, B., Yuan, S., Luo, B., Nikitin, S., Morten, J. P., Dumitru, V. A., Lienhart, W., Cunningham, E., and Wang, H.: The Global DAS Month of February 2023, Seismol. Res. Lett., 95, 1569–1577, https://doi.org/10.1785/0220230180, 2024.

Zeng, X., Lancelle, C., Thurber, C., Fratta, D., Wang, H., Lord, N., Chalari, A., and Clarke, A.: Properties of Noise Cross-Correlation Functions Obtained from a Distributed Acoustic Sensing Array at Garner Valley, California, Bull. Seismol. Soc. Am., 107, 603–610, https://doi.org/10.1785/0120160168, 2017.

https://doi.org/10.5194/essd-2025-715
Preprint. Discussion started: 13 January 2026

Open Access Earth System Science Data Discussions

Zhan, Z.: Distributed Acoustic Sensing Turns Fiber-Optic Cables into Sensitive Seismic Antennas, Seismol. Res. Lett., 91, 1–15, https://doi.org/10.1785/0220190112, 2020.

Zhu, W., Biondi, E., Li, J., Yin, J., Ross, Z. E., and Zhan, Z.: Seismic arrival-time picking on distributed acoustic sensing data using semi-supervised learning, Nat. Commun., 14, 1–11, https://doi.org/10.1038/S41467-023-43355-3, 2023.